

Photothermal Catalytic Gel Featuring Spectral and Thermal Management for Parallel Freshwater and Hydrogen Production

Minmin Gao, Connor Kangnuo Peh, Liangliang Zhu, Gamze Yilmaz, and Ghim Wei Ho*

Desalination processes often require large amounts of energy to create clean water, and vice versa for the generation of energy. This interdependence creates a tension between the two essential resources. Current research focuses on one or the other, which exacerbates water-energy stress, while few tackle both issues jointly. Herein, a low-carbon technology, H₂O–H₂ co-generation system that enables concurrent steady freshwater and clean energy output is reported. The water-energy coupled technology features a spectrally and thermally managed solar harvesting gel for photoredox and photoheating effects. This photothermal catalytic gel exploits interfacial solar heating for heat confinement, and localized plasmonic heating at the catalyst active sites to remarkably improve water and hydrogen production, thus maximizing energy value per area. To this end, a stand-alone renewable solar desalination system is successfully demonstrated for parallel production of freshwater and hydrogen under natural sunlight. By doing so, the water–energy nexus is transformed into a synergistic bond that offers opportunities to better meet expected demand rather than acting in competition.

1. Introduction

Freshwater and energy demand are set to increase due to rising population, climate changes, and economic growth as they are inextricably linked to societal development. Energy generation requires water, while freshwater production necessitates energy. The development of technology to tackle the energy crunch and/or water scarcity must manage this energy–water tension. As 97% of the earth's water is found in the ocean, desalination

plays a critical role in freshwater production. However, desalination processes often demand large electrical or thermal energy consumption. Developing energy-efficient desalination technologies is especially important for sustainable freshwater production.^[1] In recent years, solar vaporization becomes highly promising for freshwater production from seawater due to the development of solar absorber nanomaterials.^[2] These light absorbing materials can effectively harvest light and convert photon-to-thermal energy, which largely enhances the solar vaporization efficiency.^[3] Similarly, this photothermal effect has been adopted as an enhancement strategy for catalysis^[4] through extending the absorption range of photocatalysts beyond their optical bandgap to boost solar-to-chemical energy conversion. Thus far, the solar driven photothermal phenomenon demonstrates effective harvesting and utilization of solar spectrum

to stimulate photoredox and photoheating for either freshwater production or clean fuel generation separately.^[2d]

A wide range of solar absorber nanomaterials with broad-band absorption and/or localized surface plasmon resonance (LSPR) at specific wavelengths have been developed, including carbon-based materials, plasmonic metal nanoparticles, metallic oxides/nitrides, and black polymers.^[2a,b] In particular, loading plasmonic metal nanoparticles such as Au, Ag, Pt, or Pd have been found to enhance the visible light harvesting potential for photocatalytic fuel generation, increasing the activity of the original photocatalysts.^[5]

To effectively utilize the photothermal materials, current strategy is mainly achieved through confining the solar heat directly at the reaction surfaces, namely the water/air and water/catalyst interfaces in solar vaporization and photocatalysis respectively.^[2b,d,6] Nevertheless, nanoscale heat localization at the water/catalyst interface in a suspension system inevitably loses heat to the bulk liquid eventually as the catalytic materials are dispersed in the solution. The emerging designs of interfacial heating in solar vaporization ingeniously confine the photothermal materials at the water/air interface to achieve localized hot zone, which largely reduce the heat loss to bulk water.^[7] This configuration also improves light absorption as the photothermal materials are directly exposed to light without passing through other mediums. However, in most of these studies,

Dr. M. Gao, Dr. C. K. Peh, Dr. L. Zhu, Dr. G. Yilmaz, Prof. G. W. Ho
Department of Electrical and Computer Engineering
National University of Singapore
4 Engineering Drive 3, Singapore 117583, Singapore
E-mail: elehgw@nus.edu.sg

Prof G. W. Ho
Engineering Science Programme
National University of Singapore
9 Engineering Drive 1, Singapore 117575, Singapore

Prof G. W. Ho
Institute of Materials Research and Engineering
A*STAR (Agency for Science, Technology and Research)
2 Fusionopolis Way, Singapore 138634, Singapore

 The ORCID identification number(s) for the author(s) of this article can be found under <https://doi.org/10.1002/aenm.202000925>.

DOI: 10.1002/aenm.202000925

the condensation process necessary to produce clean water has often been overlooked. Placing collectors above the vaporization surface, even if transparent, often result in condensate and/or vapor interfering with the incident light harvesting.^[8] Moreover, the condensate collector will be heated up over time and reduce the condensation efficiency.^[9] Consequently, high vaporization rate cannot be simply translated into effective water harvesting. These concerns can be addressed by utilizing a hydrophobic microporous membrane to separate the feedwater and the collected water vapor, which preferentially condenses away from the light path. The hydrophobic membrane presents a barrier for the liquid-phase feedwater to pass through. The temperature difference between each side of the hydrophobic membrane creates a vapor pressure gradient, which results in vapor flux transfer across the membrane from the heated feedwater to the cold condensate side.^[1,10] By implementing the thermal localization concept using solar absorber nanomaterials will reduce the energy input for heating the feeding water, and also enlarge the temperature gradient across the membrane thereby improving its efficiency.^[9,11]

In this work, we designed a photothermal catalytic (PTC) gel with a hydrophobic membrane to realize a $\text{H}_2\text{O}-\text{H}_2$ cogeneration system (HCS) for concurrent photothermal-enhanced solar desalination and hydrogen generation. The PTC gel with broadband absorption confines heat at the PTC gel for vapor generation, while the individual plasmonic Ag nanoparticles localize heat at the catalyst active sites for hydrogen production. Complementing nanoscopic localized plasmonic heating with macroscale thermal confinement synergistically enhances both the desalination and hydrogen generation processes. The temperature difference induced by heat localization of PTC gel results in efficient vapor flux transfer across the membrane from the heated feedwater to the cold condensate side (collection chamber). This pressure gradient also drives the hydrogen generated through the membrane to the collection chamber. Moreover, the aligned microchannels of the PTC gel provide passageways to enhance the water, vapor, and hydrogen transportation and also prevent the salt crystals accumulation. A solar vaporization rate of $\approx 1.49 \text{ kg m}^{-2} \text{ h}^{-1}$ and hydrogen generation rate of $\approx 3260 \mu\text{mol m}^{-2} \text{ h}^{-1}$ under 1 sun

irradiation is achieved using the PTC gel. Subsequently, HCS is employed in the first-ever integral prototype design for parallel desalination and hydrogen energy generation. It is able to collect $\approx 5000 \text{ g m}^{-2}$ water and $\approx 4600 \mu\text{mol m}^{-2}$ hydrogen within 1 d under natural sunlight. This system with advantages of utilizing low-grade heat and treating high salinities feedwater provides an environmentally attractive and sustainable solution to resolve the tension between water and energy production.

2. Results and Discussion

A schematic drawing of the conceived HCS for photothermal vaporization and catalysis is shown in **Figure 1a**. The PTC gel is conceptually designed with photothermal and catalytic TiO_2/Ag nanofibers (NFs) and strong water absorber chitosan polymer. Accordingly, the TiO_2/Ag NFs are adapted for efficient photon-to-hydrogen conversion with porous TiO_2 NFs as the photoredox material and Ag nanoparticles as the cocatalyst for enhanced charge transfer and the plasmonic solar absorber for improved hole-scavenging activity (Figure 1a). The assembly of these functional materials into a 3D gel framework introduces beneficial structural features in light harvesting, thermal management, and mass transfer for both solar vaporization and catalysis. For one, the open gel structure enables the photoactive materials to be directly exposed to light. This resolves the prevalent issue of inefficient light absorption due to shielding effect of the upper suspending photocatalysts and light absorption/scattering of water in a typical suspension system (Figure 1b). Moreover, it also circumvents poor light penetration, especially in the case of sedimentation in the suspension system (Figure 1c).^[12] For another, the gel system warrants an effective confined interfacial heating (Figure 1d), and offers anisotropic thermal conductivity arising from the aligned pores. Such thermal confinement at macroscopic level with near-uniform temperature profile promotes greater temperature gradient across the membrane, thus leading to efficient water vaporization and hydrogen generation. Apart from facilitating directional thermal conductivity, the aligned pores provide direct vapor and gas pathways as well as water transport

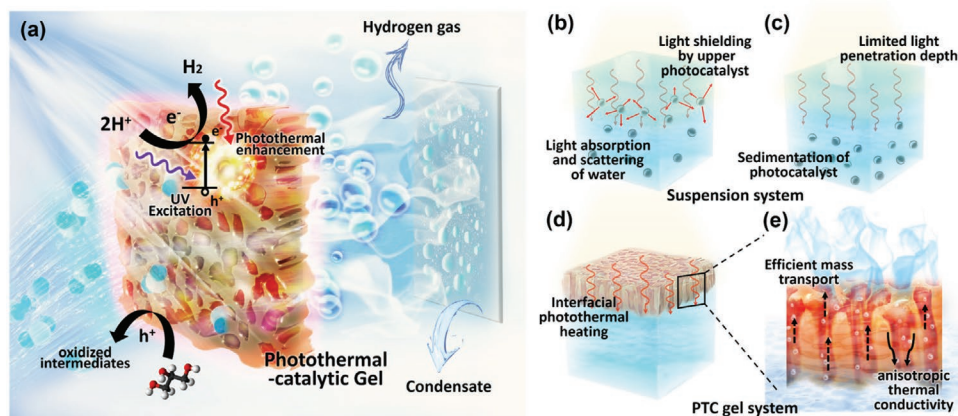


Figure 1. a) Schematic drawing of the designed PTC gel for concurrent solar vaporization and hydrogen generation. b) Inefficient light utilization in the suspension system. c) Inactive nanomaterials caused by sedimentation and light penetration. d) Interfacial photothermal heating of PTC Gel. e) Efficient mass transport and light absorption through the aligned pores within the PTC gel.

channels for efficient absorption and ion exchange of saline solution to prevent salt build up (Figure 1e).^[13] Together, the customization of catalytic, optical, thermal, and mass transport properties in an integral 3D porous PTC gel is engineered to deliver photothermal-enhanced passive solar desalination and photocatalytic hydrogen generation.

The 3D hybrid organic–inorganic nanocomposite PTC gel with aligned pores was synthesized by incorporating electrospun TiO₂/Ag NFs into chitosan with directional freezing technique, followed by freeze-drying (Figure 2a). The synthesis process is further described in the Supporting Information. TEM image reveals porous TiO₂ NFs with uniformly loaded Ag

nanoparticles (Figure 2b), evidently with a good interface and continuity between the Ag nanoparticles and TiO₂ (Figure S3, Supporting Information). The lattice fringes of 0.35 nm are attributed to the (101) of anatase TiO₂ (Figure 2f). The XRD spectrum obtained after photocatalytic reaction also suggests highly crystalline TiO₂ anatase phase with additional diffraction peaks ascribed to Ag (Figure S4, Supporting Information). The Ag nanoparticles and TiO₂ NFs amalgamation enables not only rapid charge carrier transfer during photocatalysis, but also localized plasmonic heating for photothermal-enhanced catalysis. Through the directional freezing process, the TiO₂/Ag NFs are cross-linked and well dispersed within the chitosan

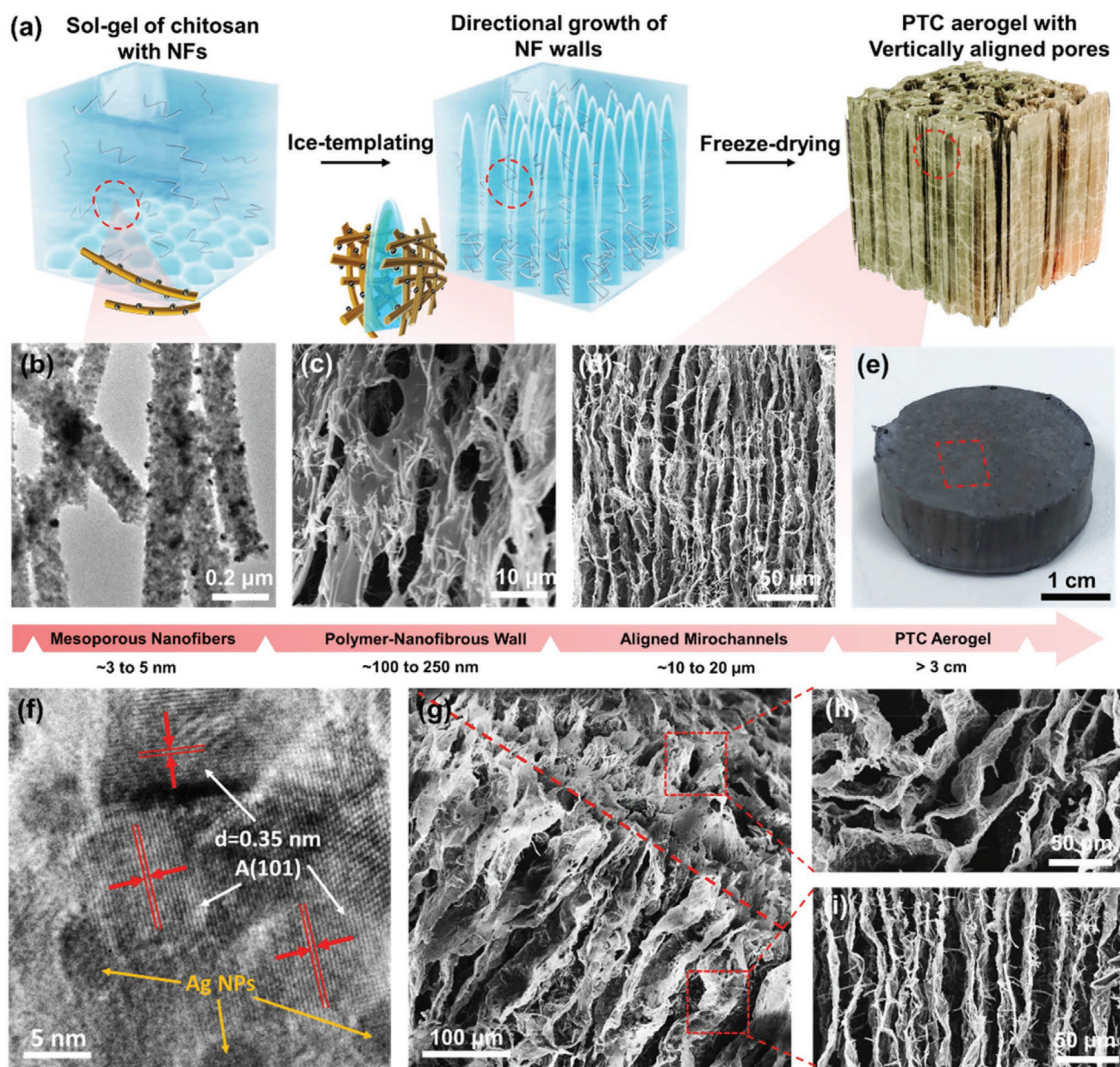


Figure 2. a) Schematic diagram of the synthesis process of the PTC gel. b) TEM image of TiO₂/Ag NFs. c-d) SEM images of the fibrous wall of PTC gel and its aligned microchannels. e) Digital photo of the as-prepared PTC gel. f) High-resolution TEM images of Ag nanoparticles within the crystalline porous TiO₂ matrix. g-i) SEM images of anisotropic microchannels in PTC gel.

polymer matrix to form polymer-nanofibrous walls (Figure 2c). The abundant natural chitosan polymer functions as a carrier for immobilization of the inorganic nanostructures as the PTC gel exhibits the characteristic FTIR bands of both chitosan gel and TiO_2/Ag NFs (Figure S5, Supporting Information). The chitosan matrix also serves as a strong water absorber medium for efficient replenishment of feedstock for both photothermal vaporization and catalysis processes.^[14] The connected walls formed the aligned microchannels with size ranging from ≈ 10 to ≈ 20 μm (Figure 2d) throughout the PTC gel. These anisotropic microchannels (Figure 2g–i) provide direct water transportation within the PTC gel and paths for the generated vapor and hydrogen to the collector. The highly porous hierarchical network of PTC gel is favorable for mass transport of both liquid and gas, additionally it also possesses large surface area with exposed active sites for efficient photocatalysis. The interconnected framework and the strong interaction between the inorganic NFs and the polymeric matrix enhance the structural stability and the mechanical strength of the PTC gel. Notably, the as-prepared gel is lightweight (Figure S6, Supporting Information) and can be made into arbitrary geometry depending on the mold used (Figure 2e and Figure S7, Supporting Information).

In order to design an efficient PTC gel for concurrent solar vaporization and photothermal-enhanced hydrogen generation, the spectral management is capitalized to promote designated solar-to-thermal and solar-to-chemical energy conversions. The

higher energy UV photons are absorbed by TiO_2 NFs for photocatalytic electron–hole pair generation. In conformity, the lower energy visible photons are captured by the Ag nanoparticles for localized surface plasmon resonance (LSPR) photothermal heating (Figure 3a), while the lowest energy infrared photons are absorbed by the PTC gel for heat generation (Figure 3b). The overall optical absorption capability of the PTC gel was characterized by total solar absorbance with the detailed calculations in the Supporting Information. PTC gel possesses the highest solar absorbance (α) of 0.95, compared with both the pure polymer chitosan gel ($\alpha = 0.25$) and the inorganic TiO_2/Ag NFs ($\alpha = 0.89$). Moreover, TiO_2/Ag NFs demonstrate a significantly higher solar absorbance, compared to intrinsic TiO_2 NFs ($\alpha = 0.28$). It can be inferred from the light absorption spectra of TiO_2/Ag and TiO_2 NFs suspension that the Ag nanoparticles exhibit strong LSPR at ≈ 475 nm (Figure 3a). These evidence the excellent light absorption capability of the TiO_2/Ag NFs after incorporating Ag nanoparticles.

Besides the broadband absorption of the PTC gel, the incorporated plasmonic Ag nanoparticles possess extraordinary photochemical conversion efficiency under resonance excitation. This capability stems from the larger light absorption cross-section than their physical size and the LSPR that confines light at nanoscale.^[2d] In this way, the localized plasmonic photothermal effect can extend the solar absorption range of the UV-active photocatalyst to markedly enhance the photocatalytic hydrogen generation performance. To demonstrate

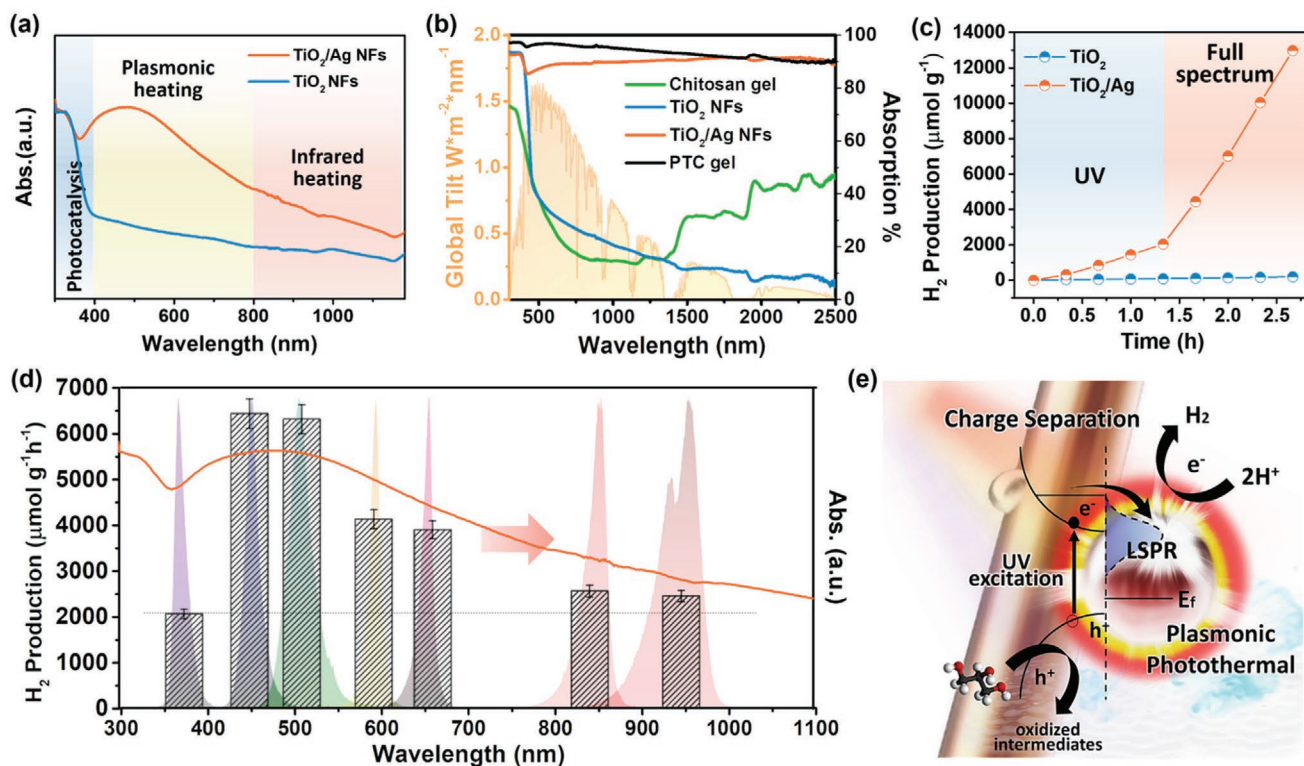


Figure 3. a) Absorption spectra of TiO_2 NFs and TiO_2/Ag NFs. b) Calculated absorption spectra of TiO_2 NFs, TiO_2/Ag NFs, chitosan gel, PTC gel, and spectral solar irradiance (AM 1.5). c) Hydrogen generation by TiO_2 NFs and TiO_2/Ag NFs in glycerol–water solution under both UV light and full spectrum irradiation. d) The photocatalytic hydrogen generation rate of the TiO_2/Ag NFs under different monochromatic light irradiation conditions, and its corresponding absorption spectrum. e) Schematic diagram of the proposed mechanism of plasmonic photothermal enhanced catalysis.

the spectral management strategy on hydrogen generation, two separate light sources, UV light (365 nm) and visible–NIR light (>400 nm) are used to validate photocatalytic activation and photothermal stimulation respectively. The TiO₂/Ag NFs sample with the optimal amount of Ag (0.15 g) (Figure S8, Supporting Information) was used to compare with intrinsic TiO₂ NFs for evaluation (Figure 3c). Under UV light irradiation, only TiO₂ was activated for photocatalytic hydrogen generation with minimum heating effect due to the mismatch of single-wavelength light source (365 nm) and the plasmonic wavelength (≈475 nm). Thus, the plasmonic inactivated Ag nanoparticles predominantly function as cocatalyst with appreciable hydrogen generation improvement from 50 μmol h⁻¹ g⁻¹ (TiO₂ NFs) to 1734 μmol h⁻¹ g⁻¹ (TiO₂/Ag NFs). Upon addition of visible–NIR light irradiation, the TiO₂/Ag NFs showed a significant enhancement of ≈395% increment (8580 μmol h⁻¹ g⁻¹) in the hydrogen generation rate under this full spectrum illumination, a stark contrast to the TiO₂ NFs of ≈62% increment. It is noted that no photocatalytic hydrogen was detected for both samples when visible–NIR light was solely used in the absence of UV light (Figure S9, Supporting Information), in accordance to the energetically insufficient photon to excite the charge carriers of TiO₂ for photoredox reaction. Hence, it can be deduced the remarkable improvement in the photocatalytic activity is attributed to the photothermal effect.

In order to further examine the plasmonic photothermal effect, another experiment was designed using various monochromatic light sources in the visible and NIR ranges. Figure 3d shows the hydrogen production of TiO₂/Ag NFs under UV (365 nm) light irradiation alone and together with another visible or NIR light source irradiation. The manifestation of the plasmonic localized heating effect within the resonance band (450 and 505 nm) of Ag nanoparticles was observed. As such, the hydrogen production rates at these two resonance wavelengths showed an enhancement of ≈208% (≈6423 μmol h⁻¹ g⁻¹) and ≈215% (≈6309 μmol h⁻¹ g⁻¹) respectively. Conversely, the hydrogen generation rates at higher wavelengths are lower than around the resonance band (≈4124 μmol h⁻¹ g⁻¹ at 593 nm and ≈3895 μmol h⁻¹ g⁻¹ at 655 nm). Due to the relatively stronger absorption coefficient of water in the NIR range, bulk heating effect presumably promotes the overall hydrogen production rate whereas the contribution from plasmonic localized heating would greatly diminish. The conformity of the hydrogen production rate with the LSPR absorption of Ag corroborates the localized plasmonic photothermal effect that plays an essential role in the enhancement of photocatalytic reactions.

On the basis of the experimental findings, the schematic of the proposed mechanism of plasmonic photothermal enhanced photocatalytic hydrogen production is shown in Figure 3e. TiO₂ NFs are UV-active photocatalyst while the incorporated Ag nanoparticles function as both the cocatalyst for better charge separation and the solar thermal collector for photothermal enhancement based on the LSPR effect. Upon full spectrum irradiation, the porous TiO₂ NFs are excited through UV light absorption to generate electron–hole pairs. The photogenerated holes are captured by the glycerol sacrificial reagent to generate H⁺ and other oxidized intermediates.^[15] In the meantime, the photogenerated electrons in the conduction band of TiO₂ are transferred to Ag nanoparticles to react with H⁺ for hydrogen

generation. Simultaneously, plasmonic photothermal heat generated by Ag nanoparticles increases the local temperature around the photocatalyst,^[16] enhancing the hole-scavenging activity that greatly improves the hydrogen production under visible–NIR light as reported in our previous works.^[2d,4,17] This photothermal effect does not only expand the solar utilization for photochemical conversion, but also promote instantaneous solar vaporization.^[4] The solar vaporization of TiO₂/Ag NFs suspension (1.05 kg m⁻² h⁻¹) outperformed the pure water vaporization (0.44 kg m⁻² h⁻¹) and TiO₂ suspension systems (0.51 kg m⁻² h⁻¹) (Figures S10 and S11a, Supporting Information). The enhancement clearly proceeds from the broadband absorption of TiO₂/Ag NFs suspension, which translates to augmented solar-to-thermal conversion, explicitly shown by the higher evaporation surface temperature (Figure S11b, Supporting Information).

The assembly of TiO₂/Ag NFs with chitosan into a PTC gel introduces additional structural advantages in terms of optical, thermal, and water wicking properties for both the photocatalytic hydrogen generation and solar vaporization. One of the drawbacks of the suspension system is the inefficient light utilization due to light shielding by the upper suspending nanomaterials, inactivity from sedimentation and light scattering by water.^[12] In view of this, the PTC gel is designed to directly and accessibly expose its active sites to light irradiation just below the water surface, thus limiting the light scattering and shielding issue (Figure 4a). Light penetration intensity against water depth at three different wavelengths were chosen to reveal the light penetration depth (Figure 4b). The light penetration depths are determined to be ≈2 cm for all wavelengths (Figure S12, Supporting Information), which indicates the PTC gel (≈0.3 cm thickness) is able to absorb all the light irradiation and fully utilize the photons for catalytic reaction (Figure S13, Supporting Information). Consequently, the PTC gel shows superior hydrogen production rates compare to other systems (Figure 4c,d). Moreover, the PTC gel performed consistently with an average hydrogen generation rate of 3208 μmol m⁻² h⁻¹ and a standard deviation of ≈2.2% for the 2 h cycling test (Figure 4c). In contrast, the hydrogen production rate of the suspension system without stirring reduced dramatically (≈66% for the first cycle and ≈94% for the fifth cycle) as the photocatalysts settle and the light absorption is reduced (Figure S14, Supporting Information). Hence, the employment of PTC gel eliminates the need for continual stirring as in the case of particulate catalyst system to assist the dispersion of the photocatalyst and the release of the hydrogen gas. Otherwise, the photocatalysts located at the bottom of the reactor are unable to harvest light irradiation effectively with limited fluid exchange for the hole-scavenging effect.^[18] However, mechanical stirring is neither practical for large-scale production nor feasible for voluminous water reactor.

Other than the desirable optical properties, the PTC gel also largely reduces the thermal mass of the system, thus effectively utilizes and distributes the thermal energy at the targeted reaction sites for both solar vaporization and photocatalysis. The solar vaporization efficiency of PTC gel system is the highest amongst other configurations (Figure 4d) pertaining to the heat confinement effect of the gel system at the air-water interface. This is verified by the higher surface temperature of PTC

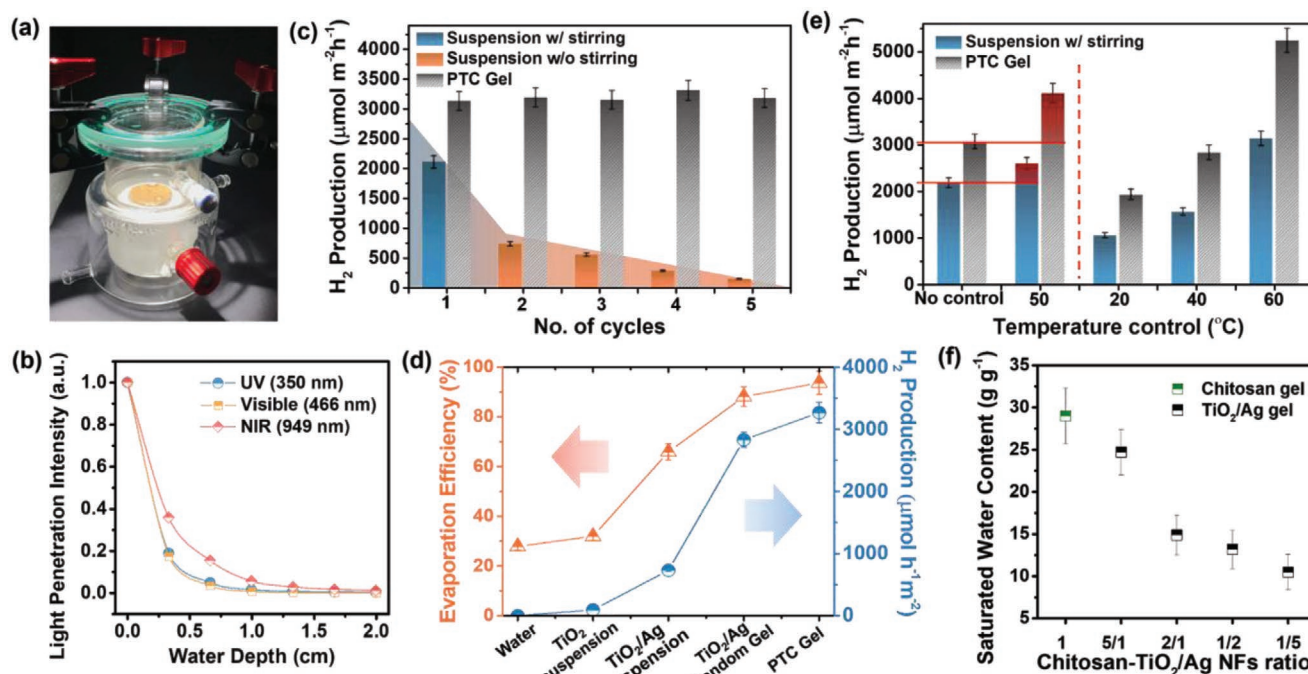


Figure 4. a) The digital photo of the reactor used for photocatalytic hydrogen production under Xe lamp irradiation. b) Light penetration intensity against water depth for selective wavelengths at 350, 466, and 949 nm. c) Hydrogen production rate of suspension system with or without stirring and PTC gel for 5 two hour cycling test. d) Summary of solar evaporation efficiency and photocatalytic hydrogen production rate of various systems. e) Hydrogen production rate of suspension system with stirring and PTC gel for various temperature conditions. f) Saturated water content in PTC gels with different composition ratios.

gel (52 °C) as shown in Figure S11 (Supporting Information). Other than macroscopic heat confinement, the localized plasmonic heating effect at nanoscale level was also demonstrated (Figure 4a). Without water circulation, comparable solution temperatures were obtained at 49.7 and 50.5 °C due to bulk heating of the suspension system and PTC gel respectively. In order to isolate the localized plasmonic photothermal effect, this bulk heating effect was normalized by keeping the solution at ≈ 50 °C through water circulation in the water jacket. It can be seen that the hydrogen production rates increased for both the suspension system and PTC gel (red highlighted portions) although the bulk solution temperatures were similar (Figure 4e). This enhancement is ascribed to localized plasmonic photothermal effect where the heat generated by the photothermal materials is mainly confined at nanoscale around the active sites, and contributed to the increase of hydrogen production. Moreover, PTC gel consistently shows high performance under various temperature conditions (Figure 4e). It was also observed that the enhancement for the PTC gel ($\approx 25.2\%$) is more than the suspension system ($\approx 16.1\%$). This is attributed to the superior nano to macroscopic heat confinement of the gel as collective heating is achieved for a reduced thermal mass, similar to the solar steam generation findings discussed earlier.

Furthermore, the PTC gel with aligned pores possesses excellent water-wicking properties. The saturated water content in the gels with various weight ratios of chitosan and TiO_2/Ag NFs was tested (Figure 4f). The composition of gel is tailored for optimal the water absorption and solar absorption in order to achieve efficient photothermal catalysis and solar vaporization concurrently.

The optimized chitosan- TiO_2/Ag NFs ratio of 2:1 with saturated water content of $\approx 15 \text{ g g}^{-1}$ is able to absorb exceeding the water needed for vaporization. Subsequently, the structure-dependent mass transport of water, vapor, or gas was evaluated by comparing the gel with random and aligned pores structures. Both of the gels with random and aligned pores achieved similar surface temperatures of 51.2 and 52 °C respectively due to similar broad absorption (Figure S15, Supporting Information). However, the gel with aligned pores provides direct open channels for water supply and vapor release, which results in higher evaporation rate of $\approx 93.8\%$ compared to the gel with random pores ($\approx 88.7\%$) as shown in Figure 4d.^[19] The effectiveness of capillary water wicking to the top surface of the gel through the aligned pores was demonstrated (Figure S16, Video S1, Supporting Information). Likewise, this aligned pores that favored mass transport also provide gas releasing channels for the photocatalytic hydrogen produced ($\approx 12\%$ enhancement) (Figure 4d). Therefore, the highly porous PTC gel with aligned pores affords high solar absorption, effective heat confinement, and rapid mass transport resulting in efficient solar vaporization and photocatalytic hydrogen generation.

In addition, the stability of the PTC gel for photocatalytic performance was further investigated under Xe lamp irradiation for 10 cycles of 2 h reaction. The hydrogen production rate remained relatively constant with fluctuation of $\approx 3\%$ as shown in Figure S17 (Supporting Information), which suggests that the PTC gel is stable for photocatalytic hydrogen production. Also, the PTC gel is easy to reuse and recycle devoid of energy intensive operations such as filtration, centrifugation etc. unlike the case of particulate photocatalysts.^[12b]

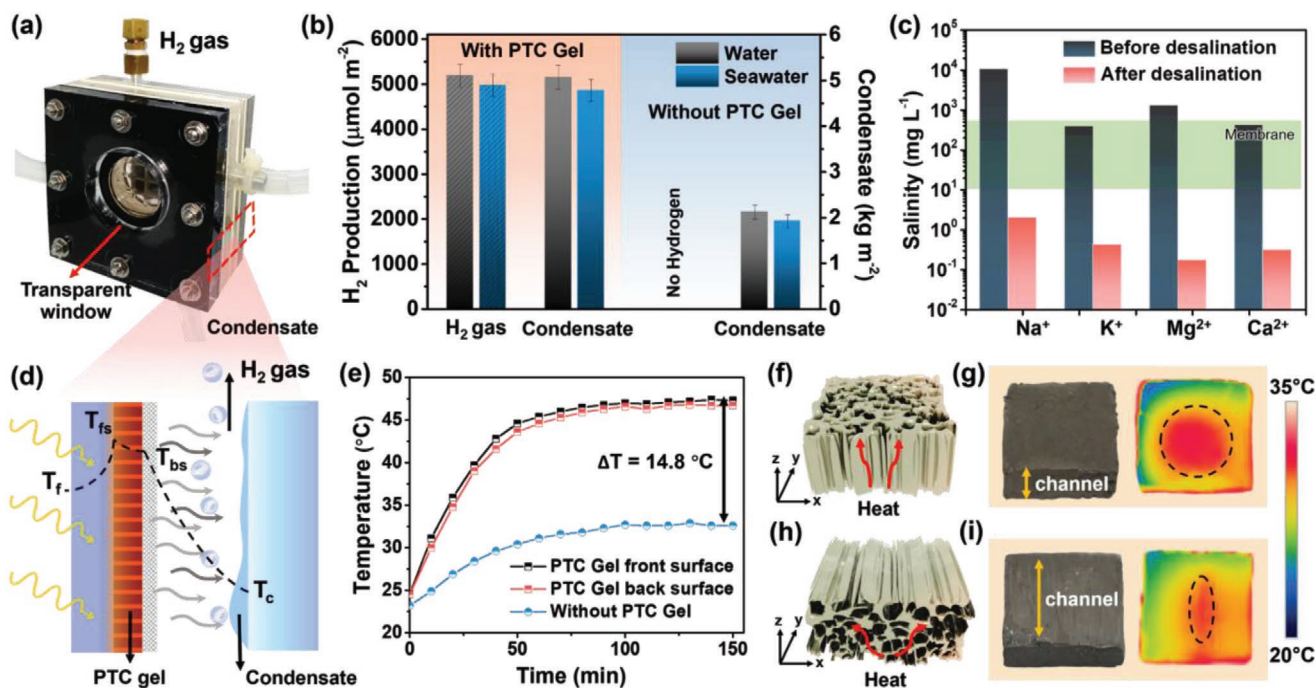


Figure 5. a) Digital photo of the custom-made device used in HCS for parallel freshwater production and hydrogen energy generation. b) Amount of hydrogen produced and condensate collected of the HCS with and without the PTC gel under Xe lamp irradiation. c) Measured salinity of four primary ions before and after solar desalination through the HCS. d) Schematic of the cross-section view of the device for HCS testing. e) Temperature profile at various points in the HCS device during the testing. f–i) Schematic representations of heat conduction through the PTC gel with respective digital photos and infrared images during the heat conduction experiment with f,g) vertical orientation and h,i) horizontal orientation, respectively.

The PTC gel was assembled onto a hydrophobic membrane (Figure S18, Supporting Information) with the macropores aligned to the transport direction (Figure S19, Supporting Information) for concurrent desalination and hydrogen generation (Figure S20, Supporting Information). Xe lamp irradiation through the transparent front window of the HCS (Figure 5a) is absorbed by the PTC gel, and only the generated vapor and hydrogen will pass through the hydrophobic membrane and are collected at the bottom and top outlets of the collector chamber separately. With the incorporation of the PTC gel, the amount of condensate collected using water and seawater sources are beyond 100% improvement (Figure 5b). The hydrogen gas generated was ≈ 5190 and ≈ 4975 $\mu\text{mol m}^{-2}$ using water and seawater respectively. The salt-rejection ability of the HCS was examined with the rejection rates of various ions (Na^+ , K^+ , Mg^{2+} , and Ca^{2+}) all over $\approx 99.9\%$ (Figure 5c), which is comparable or better than other membrane-based seawater desalination process ($10\text{--}500$ mg L^{-1}).^[20] Moreover, the collected condensate does not contain any organic material from either the gel or the sacrificial reagent (Figure S21, Supporting Information).

The enhancement in condensate collection is associated with the confined photothermal heating at the feed-membrane interface (Figure 5d). The temperature difference of the front surface (T_{fs}) with and without PTC gel is ≈ 14.8 °C and the temperature variation across the front and back surface of the membrane (T_{bs}) is also largely improved from 1.4 to 6.1 °C. (Figure 5e, Figure S22, Supporting Information). The higher temperature difference between T_{fs} and T_{bs} creates a larger vapor pressure gradient, which favors the transfer of vapor from the feed to the

collection chamber. At the same time, the air-gap between the hydrophobic membrane and the condensation plate keeps the temperature difference between T_{bs} and T_c constant at ≈ 20 °C (Figure S22, Supporting Information), which ensures continuous and efficient condensation in the collection chamber. To maintain the large temperature difference between the T_{fs} and T_{bs} , the PTC gel is devised to transfer the heat from the light exposing front surface to the back surface of the gel where the vaporization occurs with minimal loss. The oriented heat transfer ability of the PTC gel with two different anisotropic orientations (Figure 5f,h) was studied with heating source placed at the bottom of the gel (Figure S23, Supporting Information). As shown in Figure 5g, the PTC gel with aligned microchannels parallel with the heating source, thermal energy is conducted along the channel direction and confined in the z-axis direction as shown by the infrared image taken from the top view. For the PTC gel with aligned microchannels perpendicular to the heating source (Figure 5i), the infrared image reflected an elongated temperature gradient profile due to thermal conductivity in the transverse (y-axis) and longitudinal (x-axis) directions. Moreover, a lower average temperature was achieved with the PTC gel with aligned microchannels perpendicular to the heating source (Figure 5g,i). This is due to the redirecting of the absorbed heat in the y-axis and x-axis direction (Figure 5h) instead of guided transfer of heat along the z-axis direction (Figure 5f).^[7d] This validates the minimal temperature difference between the front and back surfaces of the PTC gel in the HCS (Figure 5e), as the heat can be easily conducted through the PTC gel along the direction of the aligned microchannels. Therefore,

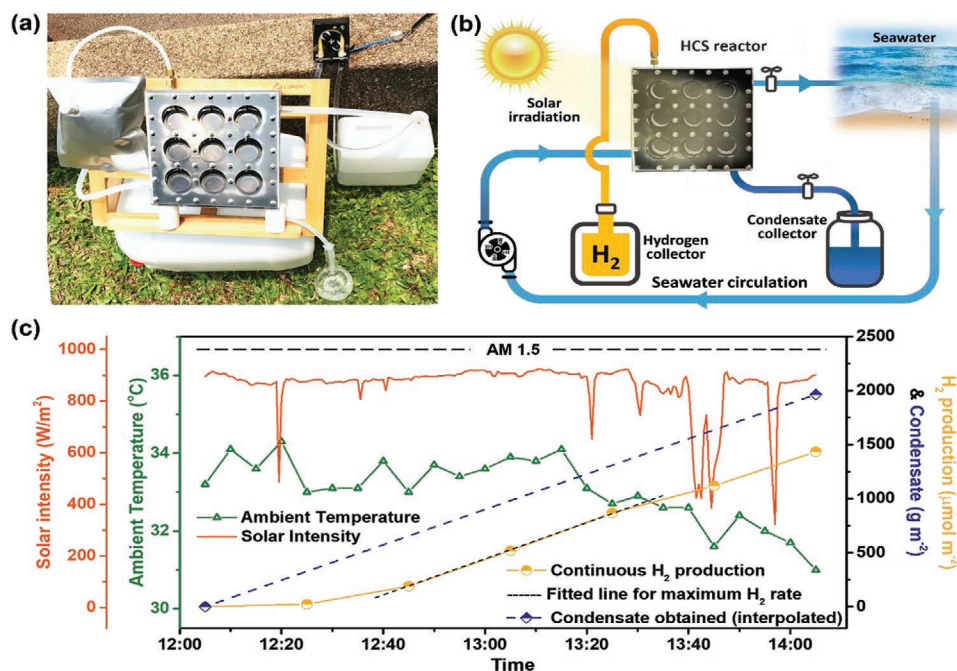


Figure 6. a) Digital photo of the set-up for outdoor testing. b) Schematic diagram and c) the measured results of the integral prototype for large-scale demonstration of concurrent photocatalysis and desalination of seawater under natural sunlight.

the PTC gel with aligned macropore pathways not just facilitate mass transfer of both liquid and gaseous phase, but also conduct heat efficiently along the aligned microchannels. The PTC gel allows heat to be produced through the photothermal conversion process which bypasses the need to perform bulk heating of the feedwater. This highly confined interfacial solar heating substantially reduces energy requirements and inherent heat loss due to large thermal mass of the bulk feedwater.

Moreover, the HCS continuously replenishes the saline feedwater, resulting in no salt accumulation in the PTC gel. Higher salt concentration in the PCT gel will back-diffuse into the feed due to the concentration differences, thus the feedwater of a wide range of salinities could be used.^[13] Various salinities with salt concentration ranging from 35 to 140 g kg⁻¹ were tested for desalination (Figure S24, Supporting Information). The amount of condensate collected was consistent with different salinities and the ICP spectrometry shows the successful removal of salt content up to ≈99.9%. It was observed that the hydrogen generation decreased at higher salinity (Figure S25, Supporting Information), possibly due to the formation of Cl radicals and subsequent reduction of the formed radicals by photoelectrons which competes with photocatalytic hydrogen generation reaction.^[2d] Moreover, the long-term stability in desalination was also tested for 10 d with steady condensate production (Figure S26, Supporting Information). The PTC gel in the HCS with strong antifouling properties is capable of treating hypersaline brines beyond the limit of reverse osmosis (≈80 g kg⁻¹),^[1] potentially used for long-term desalination.

To achieve practical desalination in real-world conditions, we have designed an integral prototype for large-scale demonstration of concurrent photocatalysis and desalination of seawater under natural sunlight. The prototype (Figure 6a) consists of a HCS reactor (Figure S27, Supporting Information), a

condensate tank connected to the condensate outlet of the HCS reactor and a gas tank with a water-vapor filter is connected to the hydrogen outlet for collecting hydrogen gas. The front transparent panel allows light to transmit through while the back of the collection chamber is circulated with seawater for cooling down the condensate plate (Figure 6b). Figure 6c shows outdoor time-dependent solar intensity, ambient air temperature under the sun and its corresponding reaction temperature, while condensate and hydrogen produced by the prototype HCS reactor were recorded accordingly. The maximum hydrogen generation rate reached as high as ≈1017 μmol m⁻² h⁻¹, while the total condensate collected was ≈1963 g m⁻². The PTC gel contributes to efficient photothermal conversion through the interfacial heating effect, as well as the plasmonic localized heating. It is able to collect ≈5000 g m⁻² water and ≈4600 μmol m⁻² hydrogen within 1 d.

3. Conclusion

The conversion and utilization of renewable solar energy for seawater solar desalination and photocatalytic fuel generation are ideal to address worldwide energy and water concerns. The PTC gel is customized with desirable broadband absorption, aligned microchannels for mass transport, good thermal conductivity, and high photocatalytic activity. Parallel condensate collection and hydrogen generation were achieved through photothermal-enhanced solar desalination and photocatalytic reactions. The PTC gel provides localized plasmonic photothermal effect at nanoscale level and confined thermal heating effect at macroscopic level, which allows synergetic enhancement in both solar desalination and photocatalytic hydrogen generation processes. The hybrid seawater solar desalination

and photocatalytic hydrogen generation HCS prototype demonstrates solar-energy-driven photothermal-enhanced hydrogen production of $\approx 4600 \mu\text{mol m}^{-2}$ and freshwater production of $\approx 5000 \text{ g m}^{-2}$ under natural sunlight irradiation in one day. The HCS can operate at high salt concentration, and with its recyclability and antifouling characteristics, provides a promising solution for off-grid or small-scale desalination and energy generation from seawater and other high salinity brines. The direct solar photothermal heating adopts renewable solar energy as the chief energy source needed for concurrent freshwater production and energy generation, transforming the tension of the water-energy nexus into a sustainable “photons” mode.

Supporting Information

Supporting Information is available from the Wiley Online Library or from the author.

Acknowledgements

This research was supported by Singapore Ministry of Education (MOE) grants (R-263-000-C85-112, R-263-000-D18-112).

Conflict of Interest

The authors declare no conflict of interest.

Keywords

desalination, hydrogen generation, photocatalysis, solar vaporization

Received: March 11, 2020

Revised: April 1, 2020

Published online: April 27, 2020

- [1] A. Deshmukh, C. Boo, V. Karanikola, S. Lin, A. P. Straub, T. Tong, D. M. Warsinger, M. Elimelech, *Energy Environ. Sci.* **2018**, *11*, 1177.
- [2] a) M. Gao, C. K. Peh, H. T. Phan, L. Zhu, G. W. Ho, *Adv. Energy Mater.* **2018**, *8*, 1800711; b) M.-Q. Yang, L. Shen, Y. Lu, S. W. Chee, X. Lu, X. Chi, Z. Chen, Q.-H. Xu, U. Mirsaidov, G. W. Ho, *Angew. Chem., Int. Ed.* **2019**, *58*, 3077; c) C. Jia, Y. Li, Z. Yang, G. Chen, Y. Yao, F. Jiang, Y. Kuang, G. Pastel, H. Xie, B. Yang, S. Das, L. Hu, *Joule* **2017**, *1*, 588; d) M. Gao, P. K. N. Connor, G. W. Ho, *Energy Environ. Sci.* **2016**, *9*, 3151; e) C. Chang, C. Yang, Y. Liu, P. Tao, C. Song, W. Shang, J. Wu, T. Deng, *ACS Appl. Mater. Interfaces* **2016**, *8*, 23412; f) J. D. Yao, Z. Q. Zheng, G. W. Yang, *Nanoscale* **2017**, *9*, 16396; g) J. Yao, Z. Zheng, G. Yang, *Nanoscale* **2018**, *10*, 2876; h) D. Ding, W. Huang, C. Song, M. Yan, C. Guo, S. Liu, *Chem. Commun.* **2017**, *53*, 6744.
- [3] a) Y. Shi, R. Li, Y. Jin, S. Zhuo, L. Shi, J. Chang, S. Hong, K.-C. Ng, P. Wang, *Joule* **2018**, *2*, 1171; b) Y. Liu, J. Chen, D. Guo, M. Cao, L. Jiang, *ACS Appl. Mater. Interfaces* **2015**, *7*, 13645; c) Y. Zeng, J. Yao, B. A. Horri, K. Wang, Y. Wu, D. Li, H. Wang, *Energy Environ. Sci.* **2011**, *4*, 4074; d) Y. Zeng, K. Wang, J. F. Yao, H. T. Wang, *Chem. Eng. Sci.* **2014**, *116*, 704; e) Y. Liu, S. Yu, R. Feng, A. Bernard, Y. Liu, Y. Zhang, H. Duan, W. Shang, P. Tao, C. Song, T. Deng, *Adv. Mater.* **2015**, *27*, 2768; f) Z. Wang, Y. Liu, P. Tao, Q. Shen, N. Yi, F. Zhang, Q. Liu, C. Song, D. Zhang, W. Shang, T. Deng, *Small* **2014**, *10*, 3234; g) Y. Wang, L. Zhang, P. Wang, *ACS Sustainable Chem. Eng.* **2016**, *4*, 1223.
- [4] L. Zhu, M. Gao, C. K. N. Peh, G. W. Ho, *Mater. Horiz.* **2018**, *5*, 323.
- [5] a) M. Wang, J. Iocozzia, L. Sun, C. Lin, Z. Lin, *Energy Environ. Sci.* **2014**, *7*, 2182; b) M. Ge, J. Cai, J. Iocozzia, C. Cao, J. Huang, X. Zhang, J. Shen, S. Wang, S. Zhang, K.-Q. Zhang, Y. Lai, Z. Lin, *Int. J. Hydrogen Energy* **2017**, *42*, 8418; c) M. Ye, J. Gong, Y. Lai, C. Lin, Z. Lin, *J. Am. Chem. Soc.* **2012**, *134*, 15720; d) D. Zheng, X. Pang, M. Wang, Y. He, C. Lin, Z. Lin, *Chem. Mater.* **2015**, *27*, 5271.
- [6] a) J.-D. Xiao, H.-L. Jiang, *Acc. Chem. Res.* **2019**, *52*, 356; b) F. L. Meng, G. Yilmaz, T. P. Ding, M. Gao, G. W. Ho, *Adv. Mater.* **2019**, *31*, 1903605; c) X. Li, J. Li, J. Lu, N. Xu, C. Chen, X. Min, B. Zhu, H. Li, L. Zhou, S. Zhu, T. Zhang, J. Zhu, *Joule* **2018**, *2*, 1331.
- [7] a) P. Yang, K. Liu, Q. Chen, J. Li, J. Duan, G. Xue, Z. Xu, W. Xie, J. Zhou, *Energy Environ. Sci.* **2017**, *10*, 1923; b) H. Ghasemi, G. Ni, A. M. Marconnet, J. Loomis, S. Yerci, N. Miljkovic, G. Chen, *Nat. Commun.* **2014**, *5*, 4449; c) H. Liu, Z. Huang, K. Liu, X. Hu, J. Zhou, *Adv. Energy Mater.* **2019**, *9*, 1900310; d) T. Li, J. Song, X. Zhao, Z. Yang, G. Pastel, S. Xu, C. Jia, J. Dai, C. Chen, A. Gong, F. Jiang, Y. Yao, T. Fan, B. Yang, L. Wågberg, R. Yang, L. Hu, *Sci. Adv.* **2018**, *4*, eaar3724; e) L. Zhou, Y. Tan, J. Wang, W. Xu, Y. Yuan, W. Cai, S. Zhu, J. Zhu, *Nat. Photonics* **2016**, *10*, 393; f) L. Zhang, B. Tang, J. Wu, R. Li, P. Wang, *Adv. Mater.* **2015**, *27*, 4889.
- [8] P. J. Alvarez, C. K. Chan, M. Elimelech, N. J. Halas, D. Villagrán, *Nat. Nanotechnol.* **2018**, *13*, 634.
- [9] G. Xue, Q. Chen, S. Lin, J. Duan, P. Yang, K. Liu, J. Li, J. Zhou, *Global Challenges* **2018**, *2*, 1800001.
- [10] J. Wu, K. R. Zodrow, P. B. Szemraj, Q. Li, *J. Mater. Chem. A* **2017**, *5*, 23712.
- [11] a) P. D. Dongare, A. Alabastri, S. Pedersen, K. R. Zodrow, N. J. Hogan, O. Neumann, J. Wu, T. Wang, A. Deshmukh, M. Elimelech, Q. Li, P. Nordlander, N. J. Halas, *Proc. Natl. Acad. Sci. USA* **2017**, *114*, 6936; b) A. Politano, P. Argurio, G. Di Profio, V. Sanna, A. Cupolillo, S. Chakraborty, H. A. Arafat, E. Curcio, *Adv. Mater.* **2017**, *29*, 1603504; c) E. Chivazzo, M. Morciano, F. Viglino, M. Fasano, P. Asinari, *Nat. Sustain.* **2018**, *1*, 763.
- [12] a) N. J. Hogan, A. S. Urban, C. Ayala-Orozco, A. Pimpinelli, P. Nordlander, N. J. Halas, *Nano Lett.* **2014**, *14*, 4640; b) M. Gao, L. Zhu, W. L. Ong, J. Wang, G. W. Ho, *Catal. Sci. Technol.* **2015**, *5*, 4703.
- [13] S. He, C. Chen, Y. Kuang, R. Mi, Y. Liu, Y. Pei, W. Kong, W. Gan, H. Xie, E. Hitz, C. Jia, X. Chen, A. Gong, J. Liao, J. Li, Z. J. Ren, B. Yang, S. Das, L. Hu, *Energy Environ. Sci.* **2019**, *12*, 1558.
- [14] H.-L. Gao, Y. Lu, L.-B. Mao, D. An, L. Xu, J.-T. Gu, F. Long, S.-H. Yu, *Mater. Horiz.* **2014**, *1*, 69.
- [15] M. Zhang, R. Sun, Y. Li, Q. Shi, L. Xie, J. Chen, X. Xu, H. Shi, W. Zhao, *J. Phys. Chem. C* **2016**, *120*, 10746.
- [16] a) M. Gao, L. Zhu, C. K. Peh, G. W. Ho, *Energy Environ. Sci.* **2019**, *12*, 841; b) M. L. Brongersma, N. J. Halas, P. Nordlander, *Nat. Nanotechnol.* **2015**, *10*, 25; c) G. Baffou, R. Quidant, F. J. García de Abajo, *ACS Nano* **2010**, *4*, 709.
- [17] C. K. N. Peh, M. Gao, G. W. Ho, *J. Mater. Chem. A* **2015**, *3*, 19360.
- [18] Y. Goto, T. Hisatomi, Q. Wang, T. Higashi, K. Ishikiriya, T. Maeda, Y. Sakata, S. Okunaka, H. Tokudome, M. Katayama, S. Akiyama, H. Nishiyama, Y. Inoue, T. Takewaki, T. Setoyama, T. Minegishi, T. Takata, T. Yamada, K. Domen, *Joule* **2018**, *2*, 509.
- [19] P. Zhang, J. Li, L. Lv, Y. Zhao, L. Qu, *ACS Nano* **2017**, *11*, 5087.
- [20] Y. Yang, R. Zhao, T. Zhang, K. Zhao, P. Xiao, Y. Ma, P. M. Ajayan, G. Shi, Y. Chen, *ACS Nano* **2018**, *12*, 829.